Atmos. Meas. Tech. Discuss., 6, 1201–1238, 2013
www.atmos-meas-tech-discuss.net/6/1201/2013/
doi:10.5194/amtd-6-1201-2013

Atmospheric Measurement Techniques Discussions

Application of ground-based hyperspectral imaging to retrieve ice crystal shape and fields of cirrus optical thickness

M. Schäfer[1], E. Bierwirth[1], A. Ehrlich[1], F. Heyner[2], and M. Wendisch[1]

[1]Leipzig Institute for Meteorology, University of Leipzig, Leipzig, Germany
[2]Thüringer Landesanstalt für Umwelt und Geologie, Jena, Germany

Received: 21 December 2012 – Accepted: 22 January 2013 – Published: 4 February 2013

Correspondence to: M. Schäfer (michael.schaefer@uni-leipzig.de)

Published by Copernicus Publications on behalf of the European Geosciences Union.

Abstract

A ground-based hyperspectral imaging spectrometer (AisaEAGLE) is applied to measure downward spectral radiance fields with high spatial (1024 spatial pixels within 36.7° field of view), spectral (488 spectral pixels, 400–970 nm, 1.25 nm full width at half maximum) and temporal (4–30 Hz) resolution. The calibration, measurement, and data evaluation procedures are introduced. A method is presented to retrieve the cirrus optical thickness τ_{ci} using ground-based spectral radiance data collected by AisaEAGLE. On the basis of four measurement cases during the second campaign of the Cloud Aerosol Radiation and tuRbulence of trade wInd cumuli over BArbados (CARRIBA) project in 2011 the spatial inhomogeneity of the investigated cirrus is characterized by the standard deviation of the retrieved τ_{ci}, as well as the width of the frequency distribution of the retrieved τ_{ci}. By comparing measured and simulated downward solar radiance as a function of scattering angle, a first estimation of the detected cirrus ice crystal shape is given and used in the retrieval of the τ_{ci}. The sensitivity of the retrieval method with respect to surface albedo, effective radius r_{eff}, cloud height, and ice crystal shape was characterized. Significant sensitivities of the retrieval method were found for the assumed surface albedo (up to 30 %) and ice crystal shape (up to 90 %). The sensitivity with regard to the effective radius (≤ 5 %) and the cloud height (≤ 0.5 %) is rather small and can be neglected.

1 Introduction

Satellite-derived cirrus cloud climatology includes cloud cover, optical thickness, and crystal effective radius. Changing either of those parameters may change the magnitude of their radiative forcing. For example, in current global circulation models a standard value of 25 µm for ice crystal effective radius is assumed. For slightly smaller crystals, cirrus clouds would have a stronger cooling effect (Garrett et al., 2003). However, cirrus clouds often show a high spatial and temporal variability and in addition might

AMTD
6, 1201–1238, 2013

be optically thin. This partly makes it hard to detect cirrus by common remote sensing techniques. The microphysical composition adds a further complication. Depending on crystal shape, the cloud radiative properties may vary substantially and cause biases in both satellite retrievals (based on reflected radiance, Eichler et al., 2009) and the energy budget (related to irradiance, Wendisch et al., 2005, 2007).

Besides crystal size and shape, the orientation of ice crystals plays a major role for both remote sensing and atmospheric energy budget studies. The spatial cirrus inhomogeneity can change the cirrus albedo by up to 25 % (over weakly reflecting surfaces and at high solar zenith angles, Carlin et al., 2002). Therefore, vertical and horizontal cloud inhomogeneities are considered to be the most probable reason for the disagreement between satellite cloud retrievals and in situ measurements. Varnai and Marshak (2001) showed that optical thickness retrievals by, e.g. MODIS (Moderate-Resolution Imaging Spectroradiometer) are biased mainly due to horizontal inhomogeneities. The reason for that is the radiative smoothing as indicated by Marshak et al. (1995) and Oreopoulos et al. (2000).

Passive satellite imaging spectro-radiometers used for cloud retrievals measure the radiance field emerging from clouds. The applicability of those data for remote sensing is limited by the aforementioned radiative smoothing and other 3-D effects, but also by the limited number of wavelength bands and spatial resolution of the sensor. A second source of uncertainty in cirrus retrievals arises from the forward simulation applied within the retrieval algorithm. In the special case of ice clouds, assumptions about the crystal shape and the corresponding scattering properties are made. Eichler et al. (2009) showed that these assumption can add an uncertainty of up to 70 % and 20 % in optical thickness and effective radius, respectively. A way to check the retrieval algorithms with respect to both horizontal cloud heterogeneity and resolution and to crystal shape is provided by flying airborne versions of spectro-radiometers above cirrus clouds, such as the MAS (MODIS Airborne Simulator). Along with extensive microphysical and solar radiation instruments as well as radiative transfer simulations Schmidt et al. (2007) and Eichler et al. (2009) investigated the differences between

AMTD
6, 1201–1238, 2013

retrieved and measured microphysical cloud properties. Schmidt et al. (2007) revealed large gaps between retrieved effective radius from MAS and simultaneous in situ measurements. This disagreement is probably related to the often discussed enhanced absorption and has not been resolved yet, partly because it has been extremely difficult to collocate remote sensing above the clouds and concurrent in-cloud microphysical measurements. Such experiments are extremely important to link satellite cloud observations of coarse resolution to spatially highly resolved measurements of cloud properties. Unfortunately, such experiments are rare, partly because instruments like MAS have been very complex and expensive, and are not available for frequent cloud experiments. Another uncertainty for cirrus retrieval from space is the assumption of surface albedo. As shown by Fricke et al. (2013) inhomogeneous surface albedo may introduce uncertainties of up to 50 % in the retrieved τ_{ci} and r_{eff}. These issues may only be solved by (I) high spatial measurements to cover cloud inhomogeneities and (II) ground based measurements less affected by surface albedo.

Furthermore, the modelling of cirrus inhomogeneities has to be improved. There are only very few cloud-resolving model studies on cirrus inhomogeneities, with regard to the radiative impact on the structure of cirrus clouds (Dobbie and Jonas, 2001), turbulence effects (Liu et al., 2003), or shear instabilities (Marsham and Dobbie, 2003). For a realistic simulation a high spatial and temporal resolution is required to represent the small-scale features of cirrus inhomogeneities. In this regard, ground-based imaging spectrometers are a helpful tool to provide information on the cirrus heterogeneity in terms of field of radiance and cirrus optical thickness.

Within this study a ground-based hyperspectral imaging spectrometer (AisaEAGLE Hanus et al., 2008) is applied to measure downward spectral radiance fields with high spatial (1024 spatial pixels within 36.7° field of view, FOV), spectral (488 spectral pixels, 400–970 nm, 1.25 nm full width at half maximum, FWHM) and temporal (4–30 Hz) resolution. Commonly AisaEAGLE is used for airborne observations of the Earth's surface and upward spectral radiance. In this paper AisaEAGLE is applied on the ground to measure downward solar radiances. In Sect. 2 the AisaEAGLE is technically

AMTD
6, 1201–1238, 2013

characterized and its calibration and data evaluation procedures are described and examplified. A method to retrieve the cirrus optical thickness τ_{ci} using AisaEAGLEs spectral radiance data is presented in Sect. 3 and applied to different cirrus cases in Sect. 4. A sensitivity study regarding the input parameters for the retrieval algorithm is given in Sect. 5.

2 Measurement of spectral radiance fields

2.1 Campaign and measurement site

In April 2011, directional and spectral measurements of downward solar radiance with the hyperspectral sensor AisaEAGLE were performed on Barbados during the second campaign of the Cloud Aerosol Radiation and tuRbulence of trade wInd cumuli over BArbados (CARRIBA) project (Siebert et al., 2012). The aim of CARRIBA was to investigate microphysical and radiative processes within and next to shallow trade wind cumuli by helicopter-borne and ground-based observations (e.g. Werner et al., 2013). However, also cirrus clouds have frequently been observed by the ground-based instrumentation.

During the CARRIBA project in 2011, the hyperspectral sensor AisaEAGLE was located in the Barbados Cloud Observatory (BCO) of the Max Planck Institute for Meteorology (Hamburg, Germany) at Deebles Point (13.15° N, 59.42° W), a cape at the east coast of Barbados.

Additionally, measurements with a Raman LIDAR and a cloud RADAR as well as radiosonde launches are available. See Siebert et al. (2012) for a more detailed description of the BCO. In parallel to the AisaEAGLE radiance measurements, all-sky images were collected every 15 s to receive informations about the cloud situation (cloud coverage, cloud type, heading).

Downward spectral radiance was measured under inhomogeneous cloud cover on 14 different days. Each day, two hours of data were collected coordinated with the

AMTD
6, 1201–1238, 2013

helicopter borne measurements. While trade wind cumuli were not always present, cirrus clouds were observed during each measurement. In the following, four measurement cases were evaluated during which where only cirrus clouds over the sky to exclude any radiative effects by low cumuli clouds.

2.2 Hyperspectral Imager AisaEAGLE

The AisaEAGLE is a commercial imaging spectrometer which is manufactured by Specim Ltd. in Finland (Hanus et al., 2008). It is a single-line sensor with 1024 spatial pixels. The instrument measures radiances in three dimensions: space, time, and wavelength. The spatial and spectral dimensions are resolved by a special set of optics that displays the image onto a two-dimensional (2-D) sensor chip. The third dimension, time, corresponds to the motion of the clouds passing over the sensor. An optical schematic for the path of the electromagnetic radiation detected by the center spatial pixel is shown in Fig. 1.

The incoming solar radiation within the field of view (FOV) of AisaEAGLE is collected by a lens (objective optics) and an entrance slit. A collimating optics direct the radiation to a grating (dispersing element) where it is split into its spectral components. The spectral components are focused on the detector which consists of a charge-coupled device (CCD) element for the spatial and spectral dimensions.

In contrast to airborne measurements (Bierwirth et al., 2012), the 2-D image evolves from the cloud movement and not from the sensor movement. The sensor was aligned perpendicularly to the direction of the cloud movement, thus 2-D images of clouds with high spatial resolution are obtained. The FOV of the AisaEAGLE depends on the lens that is used for the measurements. During the CARRIBA project in 2011, a lens with an opening angle of about 36.7° was mounted. Figure 2 shows the size of a single image pixel and the swath of the entire image as a function of cloud height.

While the swath increases with distance to the cloud by the tangens of the opening angle, the pixel size depends on its position on the sensor line. The FOV of a pixel (pixel width) in the centre (viewing zenith) is smaller than that of a pixel at the edge.

AMTD
6, 1201–1238, 2013

For example, a cloud in an altitude of 10 000 m gives an average pixel size of 6.6 m (6.3 m–6.9 m) with 6700 m swath. The "time" dimension of the hyperspectral data set also translates to a spatial quantity: the length l_{pixel} of the FOV of a pixel is the product of the perpendicular cloud velocity v_{cloud} and the selected integration time t_{int} for the measurement. Considering additionally for a non-perfect perpendicular orientation with the angle α between the flow direction of the cirrus and the orientation of the sensor line, l_{pixel} is then given by:

$$l_{\text{pixel}} = |\sin\alpha| v_{\text{cloud}} \cdot t_{\text{int}} \tag{1}$$

Figure 3 additionally illustrates the measurement geometry which is needed to derive the detected scattering angles ϑ for each spatial pixel.

The scattering angle ϑ is derived by the scalar product between the vector of the incoming solar radiation (***SC***) and the vector of the radiation scattered into the sensor direction (***CD***):

$$\cos\vartheta = \frac{\boldsymbol{CD}\cdot\boldsymbol{SC}}{|\boldsymbol{CD}|\cdot|\boldsymbol{SC}|} = \cos\varphi_0 \sin\theta_0 \sin\beta_i + \cos\theta_0 \cos\beta_i \tag{2}$$

For the calculations the solar azimuth angle φ_0 is considered relatively to the azimuth angle of the AisaEAGLE sensor line. Therefore, φ is cancelled out in the above given equation for the scattering angle ϑ.

For each spatial pixel the radiance is measured spectrally between 400 nm and 970 nm with 488 wavelength pixels. The spectral resolution is 1.25 nm FWHM.

The integration time and the measurement rate are adjustable from 0.1 ms to 200 ms and 4 s^{-1} to 30 s^{-1}, respectively. During the CARRIBA project in 2011 a frame rate of 4 Hz was used. The integration time was chosen between 10 ms and 30 ms, depending on the illumination of the cloud scene.

AMTD
6, 1201–1238, 2013

2.3 Calibration, corrections, and data handling

2.3.1 Calibration

The data collected by the AsiaEAGLE are given in counts per integration time. A calibration to obtain radiances I in units of $W m^{-2} nm^{-1} sr^{-1}$ is performed with an integrating sphere and the software AisaTools (provided by the manufacturer). The dark current is determined separately with a shutter. The calibration factors for each pixel are calculated from the calibration measurements using a certified radiance standard (integrating sphere) traceable to the National Institute of Standards and Technology.

2.3.2 Smear correction

Since the AisaEAGLE detector is based on CCD technique, it is necessary to correct for the smear effect in calibration and measurement data. The smear effect occurs during the read-out process of the collected photo-electrons which are shifted step by step from one spectral pixel to the neighbouring one into the direction of the read-out unit (Fig. 4). The read-out process is not infinitely fast. Due to the fact that radiation still can reach the sensor during the read-out, the pixels are contaminated by an additional signal. The read-out process for the larger wavelengths (red) ends earlier than the read-out for the smaller wavelengths (blue). Therefore, the additional signal (smear effect) is larger for smaller wavelengths which are longer illuminated during the read-out.

AMTD
6, 1201–1238, 2013

The measurements can be corrected for the smear effect by applying the correction algorithm:

$$
\begin{aligned}
&x_1 = y_1 \\
&x_2 - S_c \cdot y_1 = y_2 \\
&x_3 - S_c \cdot (y_1 + y_2) = y_3 \\
&\ldots \\
&x_n - S_c \cdot (\Sigma_{i=1}^{n} y_{i-1}) = y_n
\end{aligned}
\tag{3}
$$

where x_i and y_i are the uncorrected and corrected digital counts with the wavelength index $i = 1, \ldots, n$. The smear correction factor S_c is the ratio of the duration of a read-out step to the total integration time. For the first read-out step no correction is necessary, since the counts from the first pixel are shifted directly into the read-out unit. During the whole read-out process, the illumination of all pixels is assumed to remain constant. Therefore, new charges are still generated while the original charges are already shifted towards the read-out unit. The original charge from a given pixel is therefore increased by the radiation that falls on the pixel they travel through. The increase is proportional to the smear correction factor $S_c = t_{\text{read-out}}/t_{\text{int}}$, which is the ratio of the duration of one read-out step to the original integration time. This influence is increasing with the illumination brightness of the pixels (see the fourth line of Fig. 4).

The smear effect must be taken in account for each measurement, including the calibration. It should be mentioned that the AisaEAGLE CCD element consists of 1024 spectral pixels for the hypothetic wavelength range from 100 nm to 1300 nm. However, due to the optics assembly the effective spectral range of AisaEAGLE is decreased to 502 pixels in the range of 400 nm to 970 nm (so-called effective wavelength range). Spectral pixels below or above this range receive only stray light from pixels within the effective wavelength range. This makes those pixels useless for data evaluation. Tests have shown that during the smear correction the signal outside the effective wavelength range can be neglected (which greatly reduces the required data storage space). This

AMTD
6, 1201–1238, 2013

is because solar spectral radiance is typically larger for smaller (400 nm) than for larger (900 nm) wavelengths. Unfortunately this does not hold for the calibration. The halogen calibration lamp of the integrating sphere is much colder than the Sun and emits radiation with a maximum in the near infrared range (1000 nm) and low values at smaller wavelength (400 nm). Consequently, the off range wavelength pixels above 1000 nm receive a significant amount of radiation and cannot be omitted for the smear correction. If the calibration data above 1000 nm are omitted, the smear correction is not sufficient. A comparison between calibration coefficients derived with and without including the off range pixel is shown in Fig. 5. Significant differences are observed for wavelengths below 500 nm which agrees with the theory of the smear effect. Differences range from 3 % at 970 nm wavelength to 13 % at 400 nm wavelength. Therefore, it is necessary to use the entire AisaEAGLE spectral range during calibration, even though it is not used during data evaluation.

3 Retrieval of cirrus optical thickness

For the retrieval of cirrus optical thickness τ_{ci} from the measured downward spectral radiance $I_{\downarrow}$ transmitted through the cirrus, radiative transfer calculations were performed. The radiative transfer solver DISORT 2 (Discrete Ordinate Radiative Transfer) was applied. Input parameters, such as cloud optical properties, aerosol content and spectral surface albedo are provided by the library for radiative transfer calculations (libRadtran, Mayer and Kylling, 2005). The Hey parametrization by Yang et al. (2000) was used to describe the single scattering properties of ice crystals.

The simulations were performed for 530 nm which allows a comparison with available LIDAR data. Since the BCO is located at the far end of this cape, the measurement site is surrounded by half water and half rocks and grass. For simplification the surface albedo in the radiative transfer simulations was assumed to be only water, as derived by Wendisch et al. (2004) providing a value of 0.068. A maritime aerosol type was used. The cloud altitude and cloud vertical extend was determined by LIDAR

AMTD
6, 1201–1238, 2013

measurements of BCO. On the basis of the Moderate Resolution Imaging spectroradiometer (MODIS) data, a fixed effective radius r_{eff} of 20 µm was assumed. Downward solar radiance $I_{\downarrow \mathrm{cal}}$ was calculated as a function of τ_{ci}. By fitting the measured downward solar radiance $I_{\downarrow \mathrm{meas}}$ to the simulation, the corresponding τ_{ci} is interpolated. The uncertainty caused by using a fixed r_{eff}, surface albedo, cloud height, and crystal shape is analysed in a sensitivity study in Sect. 5.

The imaging measurements require an accurate description of the sensor geometry in the simulations as shown in Fig. 3. The sensor was aligned horizontally. The sensor azimuth angle was not measured directly but estimated from measurements during the time when the Sun's azimuthal position was in the direction of the sensor line. If both azimuth angles are equal, the measurements will be overexposed with a distinct maximum. The sensor azimuth angle can be derived from the time of that maximum. The viewing zenith angle is given by the sensor FOV, which is $\beta = \pm 18^{\circ}$. Related to this range, the downward solar radiance $I_{\downarrow \mathrm{cal}}$ was calculated for angles with 0.3° steps.

Figure 6 shows radiance simulations for the solar zenith angles of 30°, 45°, and 60°, a solar azimuth angle of 90° and a cirrus with ice crystals in the shape of solid columns. The base of the cirrus is in a height of 11 km.

As can be seen, the same measured radiance might lead to two different retrieval results for the cirrus optical thickness τ_{ci} e.g. for $\theta_0 = 30^{\circ}$ a radiance of $0.2\,\mathrm{W\,m^{-2}\,nm^{-1}\,sr^{-1}}$ corresponds to τ_{ci} of either 1 or 15. This ambiguity has to be solved using additional information of the estimated τ_{ci}. In case of thin cirrus (τ_{ci} less than about 3–4), the retrieval curve for low values of τ_{ci} should be used, for optically thicker cirrus the portion for large τ_{ci} should be applied. Thus independent knowledge concerning the expected range of τ_{ci} is important to avoid the ambiguity of the retrieval curve. During the CARRIBA project in 2011, this supplementary information was provided by all-sky images and LIDAR measurements. All retrieved τ_{ci} presented within this study are in the range left of the maximum of the retrieval curve presented in Fig. 6.

AMTD
6, 1201–1238, 2013

4 Measurements

4.1 Measurement cases

Four datasets of different days were evaluated: 9, 16, 18, and 23 April 2011. These days showed persistent cirrus with no other clouds below. An overview of the main characteristics of the evaluated measurement periods can be found in Table 1.

Figure 7a–d shows all-sky images from the beginning of the four cases. Within each image, the red arrow indicates the movement of the cirrus during the analysed period. The heading was derived by comparing the position of clouds in the sequence of all-sky images (15 s time resolution). The blue box indicates the area covered by the AisaEAGLE radiance measurements, the area of cirrus which is heading across the sensor line during the measurement period. Due to the fact that the AisaEAGLE was not orientated perfectly in perpendicular direction of the cirrus heading, the covered area is not a rectangle in most cases.

During all four measurement cases, τ_{ci} is estimated as lower than 3–4. That means, concerning the ambiguity of the retrieval curve given in Fig. 6, τ_{ci} is well-defined for each measurement case. The cirrus for 16 and 18 April 2011 were quit homogeneous. On 9 and 23 April 2011, a rather inhomogeneous cirrus was observed. On the 23 April 2011, a 22° halo was identified on the all-sky images but did not range into the FOV of AisaEAGLE.

Fields of transmitted downward radiance $I_{\downarrow}$ as measured by AisaEAGLE for the four cases are presented in Fig. 8. The radiance is given for 530 nm in two-dimensional colour-scale images for all 1024 spatial pixels on the abscissa and the time of measurement on the ordinate.

The cloud structure seen in the all-sky images in Fig. 7a–d is clearly imprinted in the radiance field. The average values of the measured radiance $\bar{I}_{\downarrow}$ are given in Table 1. The highest value of $\bar{I}_{\downarrow}$ was observed for 23 April 2011 and the lowest for 9 April 2011.

AMTD
6, 1201–1238, 2013

Especially for 18 April 2011 it is evident that the image is getting brighter from the left to the right side. During this day the sensor line of AisaEAGLE was orientated from north-west (pixel 1) to south-east (pixel 1024) while the solar azimuth position was in the East at the same time. This brightening is caused by enhanced scattering for small scattering angles, corresponding to the shape of the scattering phase function of ice crystals. Therefore, while performing the radiative transfer calculations to retrieve τ_{ci} it is necessary to know the exact alignment of the sensor line and the exact position of the Sun. If the sensor orientation is carefully considered, the retrieval will account for this brightness effect caused by enhanced forward scattering of ice crystals.

Using the calculated scattering angles derived for each spatial pixel from Eq. (2), Fig. 8 can be displayed as a function of scattering angle as shown in Fig. 9. The scattering angles are symmetrical for each pixels to the pixel closest to the Sun. If the Sun's azimuthal position is almost rectangular to the sensor line, a minimum appears in the detected scattering angles per spatial pixel. In such cases, the plot of $I_{\downarrow}$ as a function of the scattering angle would have overlapping sections. For clarity, one of those sections is assigned a negative sign in Fig. 8, depending on the other values. Furthermore, because of the Sun's movement during the measurement period, the images are not rectangular any more. The advantage of the illustration using scattering angles is that structures in the image related to scattering features of the ice crystals occur now in a fixed position throughout the time series as can be seen for 18 April 2011. The radiance always increases with decreasing scattering angle which is a typical characteristic of the forward scatting of ice crystals.

4.2 Retrieved ice crystal shape

Ice crystal shape can be estimated from the directional distribution of radiance considering the scattering phase function of different ice crystals. The all-sky images in Fig. 7 can be used as a first indicator. While on 9, 16, and 18 April 2011 no Halo was visible, on 23 April 2011 the typical 22° circle of enhanced radiance is present. Thus for the 23 April 2011 regular ice crystals like columns or plates must have been present. For

AMTD
6, 1201–1238, 2013

the first three cases unregular ice crystals are more likely. The directional scattering features were analysed in detail with the AisaEAGLE measurements. Figure 10 shows the average of the measured downward solar radiance $I_{\downarrow}$ as a function of scattering angle for 18 April 2011. Additionally simulations of downward radiance for different values of τ_{ci} and different ice crystal shapes are included. Figure 10a shows that for the simulations assuming rough aggregates no halo appears in the calculated radiance. However, for the calculations with solid columns, plates, as well as a mixture of ice crystals, the two halo regions are well defined in the simulation results. Furthermore, as expected, the best agreement between simulated and measured downward radiance $I_{\downarrow}$ was found for rough aggregates. For this reason, in Sect. 4.3, the τ_{ci} for 18 April 2011 were retrieved by assuming rough aggregates for the ice crystal shape.

A similar analysis for the 23 April 2011 is presented in Fig. 11. Comparible to the all-sky image enhanced radiance is measured for scattering angles of about 20° to 26°, indicating the halo. Best agreement is found for the mixture of different ice crystal shapes while for aggregates the mismatch of the halo is obvious. Since the cloud inhomogeneities during this day were rather high, an retrieval of the exact ice crystal shape is difficult. Therefore, in the following retrieval of the τ_{ci} for 23 April 2011, a mixture of ice crystals was assumed first.

For 9 April 2011 and 16 April 2011 the retrieval of ice crystal shape within the cirrus is not possible by using this method. Due to the geometry (wind direction, sensor alignment, solar position) only a narrow range of scattering angles was detected and cloud inhomogeneity was rather high. The detected scattering angles just cover the edge of the halo regions. Therefore, the radiative transfer calculations to retrieve the τ_{ci} in Sect. 4.3 were performed for solid columns first, while the uncertainties of this selection as well as for the other cases were checked in Sect. 5.

4.3 Retrieved τ_{ci}

The τ_{ci} retrieved by the presented method are displayed in Fig. 12. The unit of the abscissa and ordinate are converted into distances to the swath width and heading

AMTD
6, 1201–1238, 2013

distance of the cirrus, respectively. For this, the altitude of the cloud base was used to derive the values for the abscissa. The average wind velocity in the same altitude, derived from the National Oceanic and Atmospheric Administration (NOAA), was used to convert the ordinate into a distance.

For 18 April 2011 the retrieved τ_{ci} indicates that the cloud is very homogeneous. This confirms that the observed increase in radiance (Figs. 8 and 9) results from enhanced forward scattering of ice crystals and has been considered correctly by the model. For 23 April 2011 it can be found that quite inhomogeneous cirrus was observed with large areas of clear-sky regions in between.

Frequency distributions of the retrieved τ_{ci} for each measurement day are shown in Fig. 13. The histograms are normalized by the total of the retrieved τ_{ci} with a bin size of 0.05 in τ_{ci}. The average and the standard deviation of the retrieved τ_{ci} for each dataset are additionally listed in Table 1. High standard deviations compared to the average values are a further measure for the homogeneity of the detected cloud situation. Thus, the AisaEAGLE measurements confirm that the cirrus on 16 and 18 April 2011 was more homogeneous than on 9 and 23 April 2011.

5 Sensitivity study

A sensitivity study was performed to quantify the retrieval uncertainties with regard to the assumptions made on the model input parameter. Besides surface albedo, cloud properties such as the effective radius r_{eff} of the cirrus ice crystals, the cloud height and vertical extent, as well as the ice crystal shape were considered.

For the sensitivity study all input parameters of the benchmark retrieval (BM) except one were kept constant. The sensitivity is expressed as the relative difference between the results of the sensitivity study, calculated using the average values of τ_{ci} (indicated by $\bar{\tau}_{ci}$). The results are listed in Table 2.

AMTD
6, 1201–1238, 2013

$$\Delta\bar{\tau}_{\mathrm{ci}} = 100\,\% \cdot \left(\frac{\bar{\tau}_{\mathrm{ci,BM}} - \bar{\tau}_{\mathrm{ci}}}{\bar{\tau}_{\mathrm{ci,BM}}} \right) \quad (4)$$

The benchmark case used a surface albedo of water (0.068 at 530 nm wavelength). Due to the fact that AisaEAGLE was not surrounded by water only but also by grass and sand, possible uncertainties may occur in the retrieval results. To quantify those uncertainties the retrieval was repeated using the surface albedo for grass and sand (0.073 and 0.314), respectively (Feister and Grewe, 1995). The effective radius r_{eff} was assumed to be 20 µm in the benchmark retrieval. The sensitivity study was performed for 15 µm and 40 µm. This range was estimated from MODIS measurements. The cirrus optical thickness τ_{ci} was too low to be detectable by MODIS during the period of the presented measurements. Therefore, the surrounding regions of Barbados were used to derive the range of the effective radii.

Another source for uncertainties is the cloud height and vertical extent. For the sensitivity tests the cloud was lifted 4 km upward and 4 km downward; the cloud vertical extent was not changed.

For ground-based measurements and without in situ observations it is impossible to determine directly the ice crystal shape within the cirrus. While for the benchmark retrieval solid columns were assumed, the sensitivity study was performed with plates and rough aggregates.

The differences between the benchmark retrieval and the sensitivity study vary in a range from less than one percent up to almost 90 % dependent on the input parameter. While Table 2 gives the different averages over the entire scene, in Fig. 14 the uncertainties based on pure simulations are shown. Here, radiance were simulated for cirrus in the range τ_{ci} 0 to 0.5 and variable surface albedo, r_{eff}, height and crystal shape. The simulated radiance are then applied to the retrieval method where the benchmark properties are assumed.

Table 2 shows that for a higher surface albedo τ_{ci} will be overestimated. For a grass surface with a slightly higher albedo than for water (0.068 and 0.073, respectively), the

AMTD
6, 1201–1238, 2013

overestimation is still small. The calculations for sand (0.378) show a strong overestimation of τ_{ci}. With a maximum of almost 29 % on 18 April 2011 and a minimum of around 21 % on 16 April 2011, the uncertainties are larger than those arising from the measurement uncertainty. This indicates that the surface albedo has to be determined in advance to guarantee reliable measurements of τ_{ci}. This relation can also be found in Fig. 14a. The retrieved τ_{ci} for the synthetic radiance above water and grass are almost identical. Compared to this, the retrieval curve for sand shows higher values. The overestimation of up to 30 % seems to be relatively high, e.g. for very small τ_{ci} the percental difference can be quit large. However, looking at the retrieved τ_{ci} for the sensitivity study in Fig. 14a and the absolute values in Table 2, the difference in τ_{ci} is just about ±0.1 and lower. This sensitivity study represents an extreme case, as the grass at Deebles Point was patchy and rather dry, so the literature estimate for the surface albedo is on the high side.

The downward solar radiance $I_{\downarrow}$ depends approximately linearly on the ice crystals r_{eff}. For the investigated cases during this study it can be seen that for a smaller r_{eff} the retrieved τ_{ci} will be underestimated. For a larger r_{eff} the retrieved τ_{ci} will be overestimated. Looking at the differences listed in Table 2 linearity can be assumed. The absolute difference of $r_{eff} = 40\,\mu m$ referring to $r_{eff} = 20\,\mu m$ is four times higher than for $r_{eff} = 15\,\mu m$ referring to $r_{eff} = 20\,\mu m$. This ratio approximately is found for the calculated differences in Table 2. However, comparing the results given in Table 2 and the retrieval curve shown in Fig. 14b, the differences are in a range below 5 %. This can also be seen in the non-significant change in the absolute values. Therefore, the uncertainty caused by estimating the unknown value of r_{eff} can be neglected.

Furthermore, it was found that there is no significant dependence of the retrieved τ_{ci} on the cloud height. The differences for all four cases are below 1 %. Only on 18 April 2011, the difference is slightly larger with an underestimation of less than 1 %. Therefore, possible uncertainties of the retrieved τ_{ci} due to the cloud height are negligible. This is also reproducible while looking on the retrieval curves in Fig. 14c which are

AMTD
6, 1201–1238, 2013

congruent. The first variation of the absolute value of τ_{ci} occurs at the third position after the decimal point.

The final parameter for which the sensitivity of the retrieval algorithm was tested is the ice crystal shape. As seen in Table 2, the differences show values up to almost 90 % in the measured cirrus fields. The retrieved τ_{ci} in Fig. 14d confirm this statement. Compared to the other parameters, the retrieval curves show larger differences to each other. In the region of the detected τ_{ci} from the four presented measurement cases, the differences between the curves increase with increasing τ_{ci}. By using plates or rough aggregates instead of solid columns, τ_{ci} will be underestimated in both cases. The average of τ_{ci} is larger by up to 0.2. Compared to the average values of the detected τ_{ci} this is not negligible. Therefore, improvements in the determination of the ice crystal shape are important.

6 Summary and conclusions

Downward solar radiance fields were measured with high spatial, spectral and temporal resolution with a hyperspectral imaging spectrometer, AisaEAGLE. The procedure of data evaluation (dark current correction, smear correction) was described. It was shown that the dark current and smear correction must be taken into account for every measurement (calibration included). During the calibration procedure the whole spectral range (100–1300 nm) must be used for an accurate smear correction.

The cirrus optical thickness τ_{ci} is retrieved from the radiance measurements. On the basis of four measurement cases collected during the CARRIBA project in 2011 on Barbados, the feasibility of retrieving cirrus optical thickness at high spatial resolution and characterizing the cirrus heterogeneity was demonstrated. The cirrus on 16 and 18 April 2011 was quite homogeneous with mean τ_{ci} of 0.28 and 0.20 and coefficients of variation of 0.09 and 0.03 showed quite homogeneous cirrus, while on 9 and 23 April 2011 rather inhomogeneous cirrus with mean τ_{ci} of 0.41 and 0.30 and coefficients of variation of 0.17 and 0.20 was observed.

AMTD
6, 1201–1238, 2013

It was found that the homogeneity of the investigated cirrus is represented by the standard deviation of the retrieved τ_{ci}.

The sensitivity of the retrieval method was characterized by varying the model input parameters such as surface albedo, the effective radius, the cloud height and the ice crystal shape. Significant sensitivities of the retrieval method have been found with respect to the surface albedo and the ice crystal shape with up to 30 % and 90 % differences, respectively. The sensitivity of the effective radius (≤ 5 %) and the cloud height (≤ 0.5 %) is rather small and can be neglected. This indicates that accurate knowledge about surface albedo and ice crystal shape is required to derive reliable cirrus optical thickness with AisaEAGLE. However, the determination of the ice crystal shape is complicated without in situ measurements inside the cirrus. Due to the fact that AisaEAGLE is able to measure radiance as a function of a wide range of calculable scattering angle, it gives the opportunity to receive information about the scattering phase function from the radiance measurements. A first estimate of ice crystal shape was retrieved by comparing the directional radiance measured by AisaEAGLE to simulation and analysing the all-sky images. By this, it was possible to distinguish between regular ice crystals producing a typical 22° halo and irregular ice crystals without halo. The shape retrieval was limited to the narrow range of scattering angles which did not cover the halo in some cases. In future studies the detected scattering angle range will be increased, using a scanning version of the AisaEAGLE. The results will then be implemented in the retrieval algorithm to allow cirrus retrieval independent on any assumption of ice crystal shape.

To adjust the measurement set up for this purpose, the best way to operate AisaEAGLE in a ground-based application is to adjust the sensor line into the azimuthal direction of the Sun, with the clouds heading perpendicularly across the sensor line. Performing the measurements like this, the maximum possible range of the scattering phase function as well as the maximum possible range of the cloud field can be detected without a spatial distortion of the cloud shape.

AMTD
6, 1201–1238, 2013

Acknowledgements. We are grateful for funding of project SI 1534/3-1 and WE 1900/18-1 by Deutsche Forschungsgemeinschaft within the framework of CARRIBA. The authors thank the Institute for Tropospheric Research, Leipzig, particularly Holger Siebert and the Max Planck Institute Hamburg for organising the campaign and the logistic support at BCO.

References

Bierwirth, E., Ehrlich, A., Wendisch, M., Gayet, J.-F., Gourbeyre, C., Dupuy, R., Herber, A., Neuber, R., and Lampert, A.: Optical thickness and effective radius of Arctic boundary-layer clouds retrieved from airborne spectral and hyperspectral radiance measurements, Atmos. Meas. Tech. Discuss., 5, 7753–7781, doi:10.5194/amtd-5-7753-2012, 2012. 1206

Carlin, B., Fu, Q., Lohmann, U., Mace, G. G., Sassen, K., and Comstock, J. M.: High-cloud horizontal inhomogeneity and solar albedo bias, J. Climate, 15, 2321–2339, 2002. 1203

DellEndice, F., Nieke, J., Koetz, B., Schaepman, M. E., and Itten, K.: Improving radiometry of imaging spectrometers by using programmable spectral regions of interest, ISPRS J. Photogramm., 64, 632–639, doi:10.1016/j.isprsjprs.2009.05.007, 2009. 1225

Dobbie, S. and Jonas, P.: Radiative influences on the structure and lifetime of cirrus clouds, Q. J. Roy. Meteor. Soc., 127, 2663–2682, 2001. 1204

Eichler, H., Ehrlich, A., Wendisch, M., Mioche, G., Gayet, J.-F., Wirth, M., Emde, C., and Minikin, A.: Influence of ice crystal shape on retrieval of cirrus optical thickness and effective radius: a case study, J. Geophys. Res., 114, D19203, doi:10.1029/2009JD012215, 2009. 1203

Feister, U. and Grewe, R.: Spectral albedo measurements in the UV and visible region over different types of surfaces, Photocem. Photobiol., 62, 736–744, doi:10.1111/j.1751-1097.1995.tb08723.x, 1995. 1216

Fricke, C., Ehrlich, A., Jäkel, E., Bohn, B., Wirth, M., and Wendisch, M.: Influence of surface albedo heterogeneity on passive remote sensing of cirrus properties, Atmos. Chem. Phys., in press, 2013. 1204

Garrett, T. J., Gerber, H., Baumgardner, D. G., Twohy, C. H., and Weinstock, E. M.: Small, highly reflective ice crystals in low-latitude cirrus, Geophys. Res. Lett., 30, 2132, doi:10.1029/2003GL018153, 2003. 1202

AMTD
6, 1201–1238, 2013

Hanus, J., Malenovsky, Z., Homolova, L., Veroslav, K., Petr, L., and Pavel, C.: Potentials of the VNIR airborne hyperspectral system AISA Eagle, in: Symposium GIS Ostrava, CZ, 2008. 1204, 1206

Liu, H.-C., Wang, P., and Schlesinger, R.: A numerical study of cirrus clouds. Part II: Effects of ambient temperature, stability, radiation, ice microphysics, and microdynamics on cirrus evolution, J. Atmos. Sci., 60, 1097–1119, 2003. 1204

Marshak, A., Davis, A., Wiscombe, W., and Cahalan, R. F.: Radiative smoothing in fractal clouds, J. Geophys. Res., 100, 26247–26261, 1995. 1203

Marsham, J. and Dobbie, S.: The effects of wind shear on cirrus: a large-eddy model and radar case-study, Q. J. Roy. Meteor. Soc., 131, 2937–2955, 2003. 1204

Mayer, B. and Kylling, A.: Technical note: The libRadtran software package for radiative transfer calculations – description and examples of use, Atmos. Chem. Phys., 5, 1855–1877, doi:10.5194/acp-5-1855-2005, 2005. 1210

Oreopoulos, L., Marshak, A., Cahalan, R. F., and Wen, G. Y.: Cloud three-dimensional effects evidenced in Landsat spatial power spectra and autocorrelation functions, J. Geophys. Res., 105, 14777–14788, 2000. 1203

Schmidt, K. S., Pilewskie, P., Platnick, S., Wind, G., Yang, P., and Wendisch, M.: Comparing irradiance fields derived from Moderate Resolution Imaging Spectroradiometer airborne simulator cirrus cloud retrievals with solar spectral flux radiometer measurements, J. Geophys. Res., 112, D24206, doi:10.1029/2007JD008711, 2007. 1203, 1204

Siebert, H., Bethke, J., Bierwirth, E., Conrath, T., Dieckmann, K., Ditas, F., Ehrlich, A., Farrell, D., Hartmann, S., Izaguirre, M. A., Katzwinkel, J., Nuijens, L., Roberts, G., Schäfer, M., Shaw, R. A., Schmeissner, T., Serikov, I., Stevens, B., Stratmann, F., Wehner, B., Wendisch, M., Werner, F., and Wex, H.: The fine-scale structure of the trade wind cumuli over Barbados – an introduction to the CARRIBA project, Atmos. Chem. Phys. Discuss., 12, 28609–28660, doi:10.5194/acpd-12-28609-2012, 2012. 1205

Varnai, T. and Marshak, A.: Statistical analysis of the uncertainties in cloud optical depth retrievals caused by three-dimensional radiative effects, J. Atmos. Sci., 58, 1540–1548, 2001. 1203

Wendisch, M., Pilewskie, P., Jäkel, E., Schmidt, S., Pommier, J., Howard, S., Jonsson, H. H., Guan, H., Schröder, M., and Mayer, B.: Airborne measurements of areal spectral surface albedo over different sea and land surfaces, J. Geophys. Res., 109, D08203, doi:10.1029/2003JD004392, 2004. 1210

AMTD
6, 1201–1238, 2013

Wendisch, M., Pilewskie, P., Pommier, J., Howard, S., Yang, P., Heymsfield, A. J., Schmitt, C. G., Baumgardner, D., and Mayer, B.: Impact of cirrus crystal shape on solar spectral irradiance: a case study for subtropical cirrus, J. Geophys. Res., 110, D03202, doi:10.1029/2004JD005294, 2005. 1203

Wendisch, M., Yang, P., and Pilewskie, P.: Effects of ice crystal habit on thermal infrared radiative properties and forcing of cirrus, J. Geophys. Res., 112, D08201, doi:10.1029/2006JD007899, 2007. 1203

Werner, F., Siebert, S., Pilewskie, P., and Wendisch, M.: Helicopter-borne passive remote sensing and collocated in situ observations of microphysical and optical properties of trade wind cumuli under overlying cirrus, J. Geophys. Res.-Atmos., in review, 2013. 1205

Yang, P., Liou, K. N., Wyser, K., and Mitchell, D.: Parameterization of the scattering and absorption properties of individual ice crystals, J. Geophys. Res., 105, 4699–4718, 2000. 1210

AMTD
6, 1201–1238, 2013

Table 1. Characteristics of the evaluated measurement periods.

	9 April	16 April	18 April	23 April
Start time (UTC)	13:26	13:43	13:43	16:45
Average θ_0 (°)	36.7	28.6	28.5	14.5
Cirrus flow direction	SW → NE	NW → SE	WSW → ENE	SSW → NNE
Appearance	inhomogeneous	homogeneous	homogeneous	inhomogeneous
Cloud height (km)	11–15	12–15	13–15	11–14
$\bar{I}_\mathrm{l}$ ($\mathrm{W\,m^{-2}\,nm^{-1}\,sr^{-1}}$) $\pm\sigma$	0.08 ± 0.02	0.11 ± 0.02	0.10 ± 0.03	0.16 ± 0.03
$\bar{\tau}_\mathrm{ci} \pm \sigma$	0.41 ± 0.17	0.28 ± 0.09	0.20 ± 0.03	0.30 ± 0.20
Covered ϑ range (°)	35.1–47.1	32.6–37.9	21.2–48.2	12.2–36.3

AMTD
6, 1201–1238, 2013

Table 2. Relative (%) and absolute difference of retrieved τ_{ci} in comparison to benchmark case.

	9		16		18		23	
	rel.	abs.	rel.	abs.	rel.	abs.	rel.	abs.
Surface albedo (grass)	2.6	0.01	0.4	0.00	0.6	0.00	0.51	0.00
Surface albedo (sand)	27.8	0.11	20.6	0.06	28.9	0.06	23.27	0.21
r_{eff} (15 µm)	0.5	0.00	1.1	0.00	0.5	0.00	−0.6	−0.00
r_{eff} (40 µm)	−4.9	−0.02	−3.9	−0.01	−0.9	−0.00	−0.58	−0.00
Cloud height (lower)	−0.45	−0.00	−0.28	−0.00	−0.14	−0.00	−0.38	−0.00
Cloud height (higher)	0.31	0.00	0.19	0.00	−0.05	0.00	0.34	0.00
Crystal shape (plates)	14.80	0.06	75.3	0.21	85.6	0.17	64.06	0.58
Crystal shape (r.-aggr.)	23.3	0.09	26.1	0.07	33.1	0.07	14.37	0.13

AMTD
6, 1201–1238, 2013

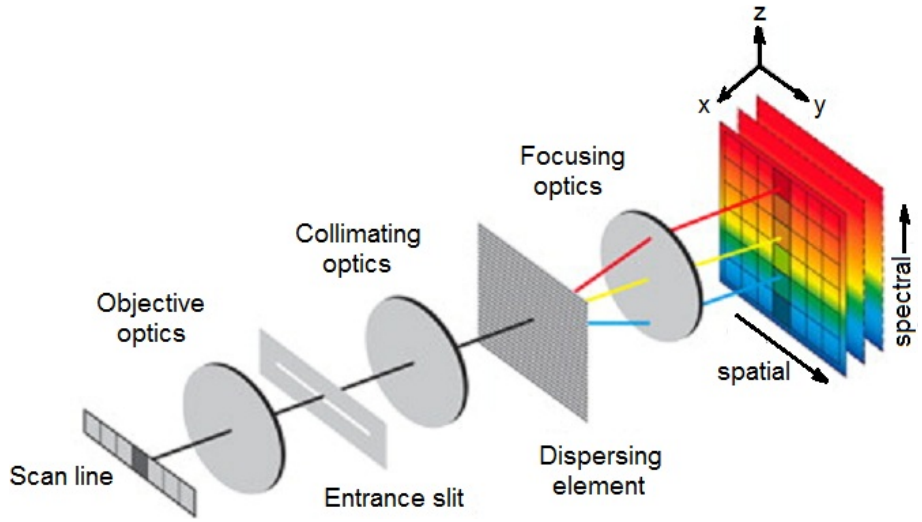

Fig. 1. Optical scheme of an imaging spectrometer. Adapted from DellEndice et al. (2009).

AMTD
6, 1201–1238, 2013

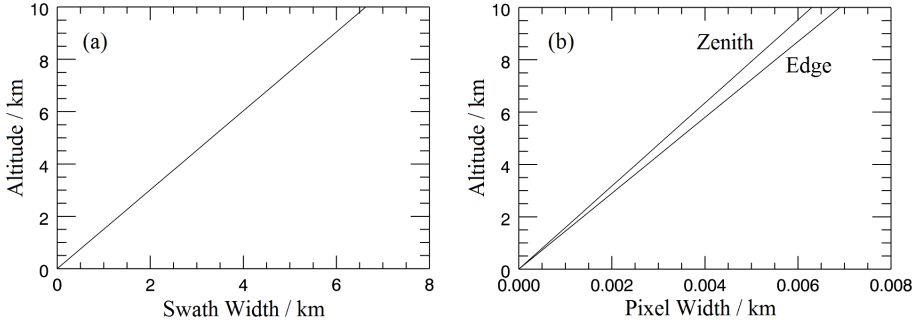

Fig. 2. Characteristic **(a)** swath and **(b)** pixel width for AisaEAGLE using the 36.7° lens.

AMTD
6, 1201–1238, 2013

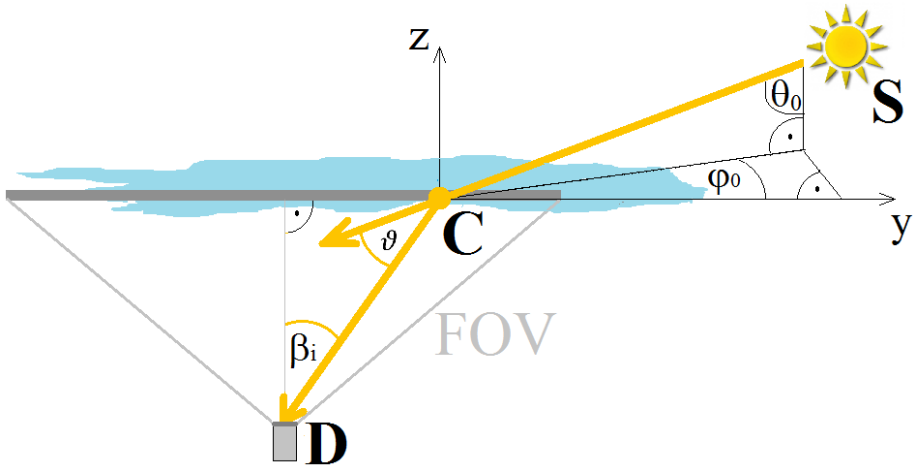

Fig. 3. Illustration of the AisaEAGLE measurement geometry in a Cartesian coordinate system (x, y, z) with position of the Sun (S), a scattering cloud particle (C) and the AisaEAGLE detector (D). θ_0 is the solar zenith angle, φ_0 the solar azimuth angle, ϑ the scattering angle, and β_i the viewing angle of the corresponding pixel.

AMTD
6, 1201–1238, 2013

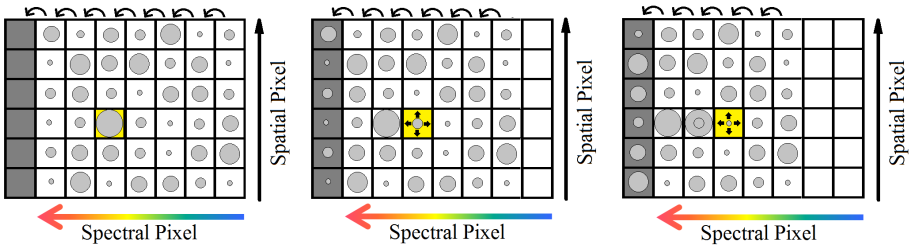

Fig. 4. Illustration of the read-out process and the smear effect. The grey bar on the left side illustrates the read-out unit. The arrows indicate the shifting direction of the photo-electrons. The magnitude of the signal of each pixel is indicated by the size of the circles. The smear effect is illustrated for one spatial pixel which is exposed to additional illumination at one spectral pixel (yellow) during the read-out process.

AMTD
6, 1201–1238, 2013

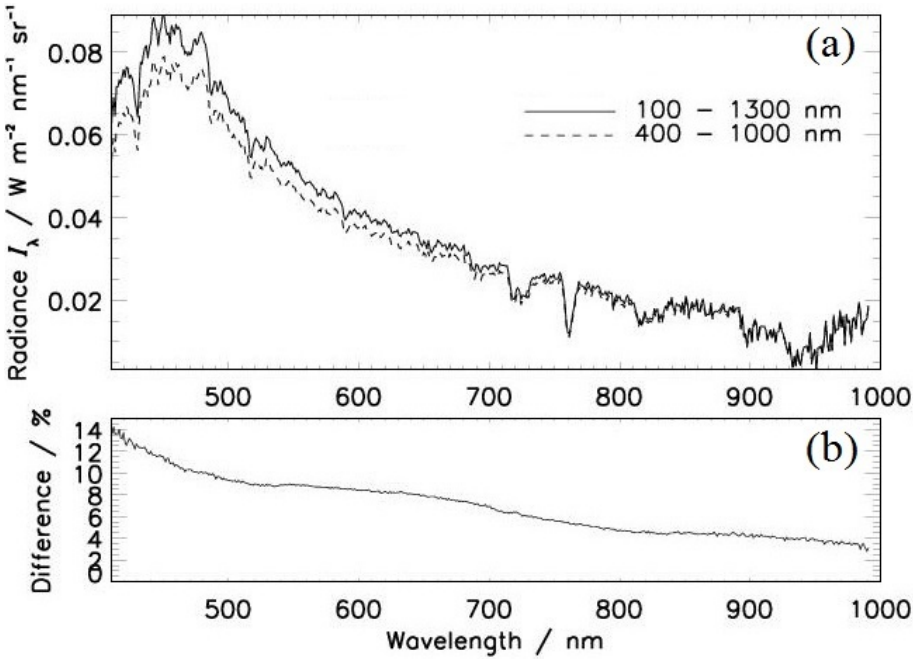

Fig. 5. (a) Spectral radiance measured with AisaEagle, for smear corrections considering different wavelength intervals in the calibration, 100–1300 nm (solid line), 400–1000 nm (dashed line). **(b)** Differences between the spectral radiances shown in panel **(a)**.

AMTD
6, 1201–1238, 2013

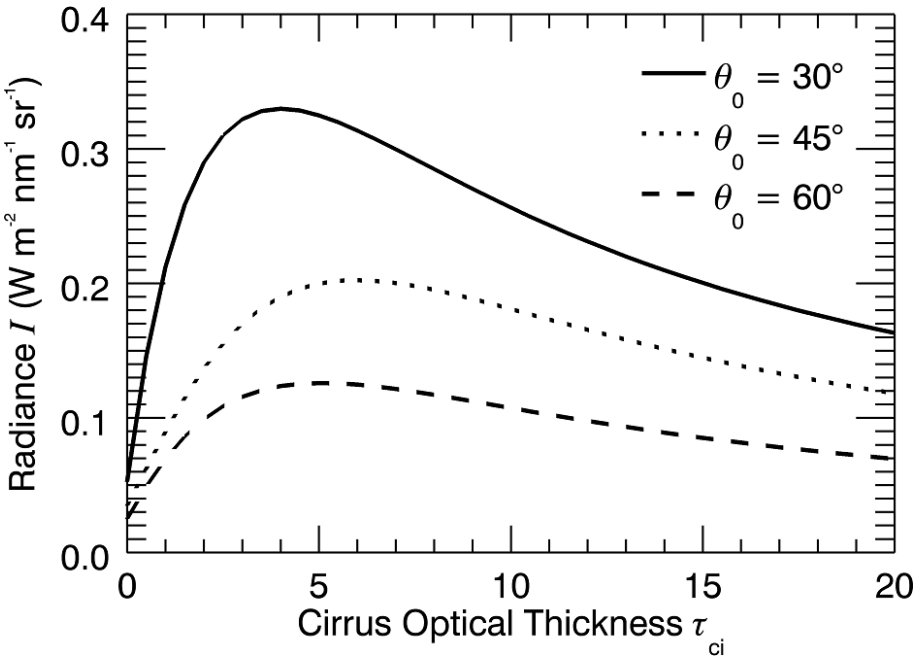

Fig. 6. Simulated radiance at 530 nm as a function of cloud optical thickness to illustrate the ambiguity of the retrieval results.

AMTD
6, 1201–1238, 2013

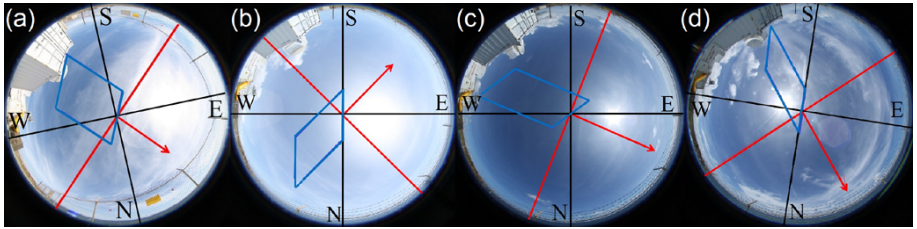

Fig. 7. All-sky image from the beginning of the evaluated AisaEAGLE radiance measurements, flow direction of the cirrus (red arrow) and FOV of the AisaEAGLE radiance measurements (blue). Orientation given by black lines and capital letters.

AMTD
6, 1201–1238, 2013

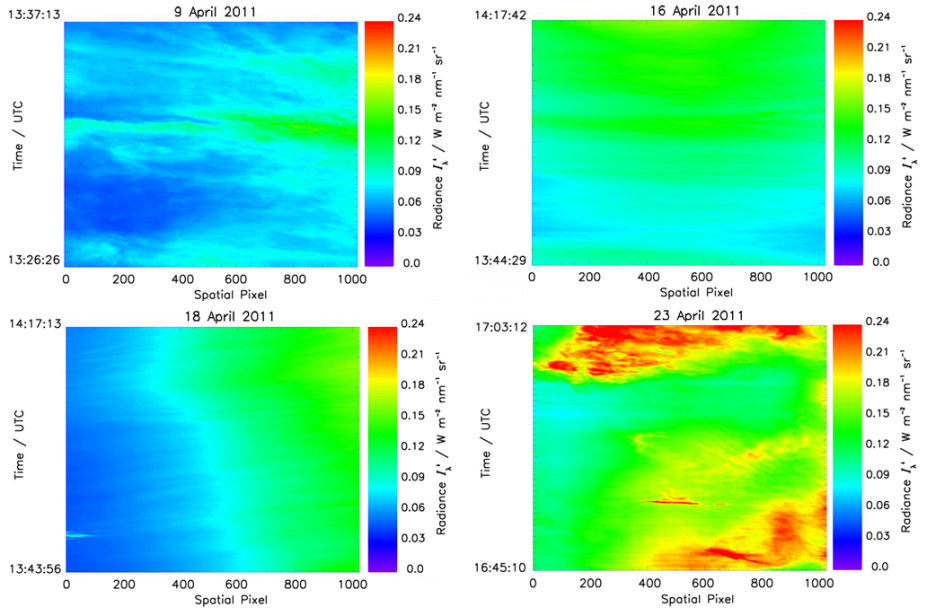

Fig. 8. Two-dimensional images of the evaluated AisaEAGLE radiance measurements at 530 nm with the measured $I_\downarrow$ (W m^{-2} nm^{-1} sr^{-1}) given in colour scales.

AMTD
6, 1201–1238, 2013

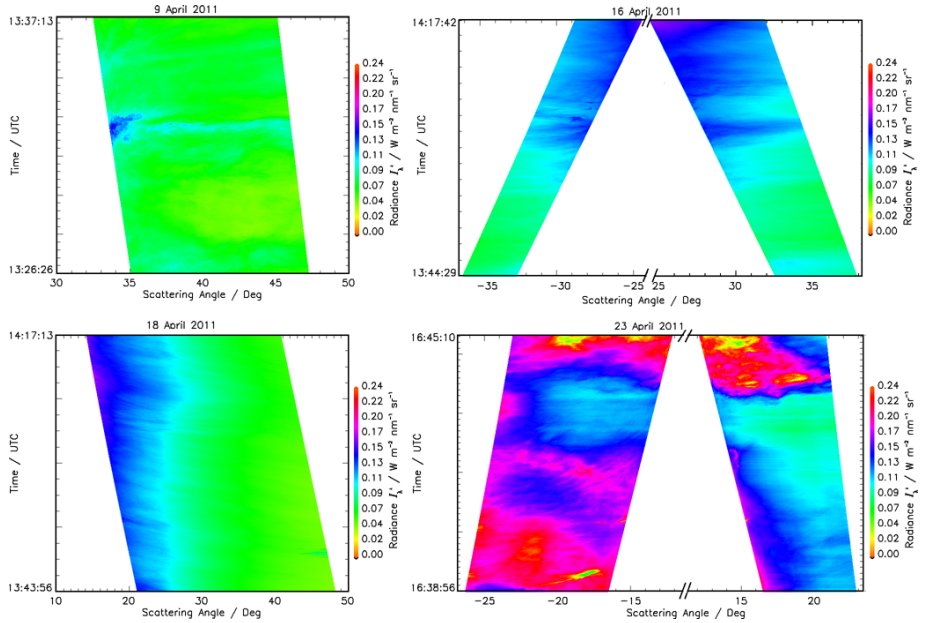

Fig. 9. Time series of the measured downward solar radiance $I_\downarrow$ during the four measurement cases as a function of scattering angle for each spatial pixel. The range of the abscissa of each image is fitted to the corresponding range of covered scattering angles.

AMTD
6, 1201–1238, 2013

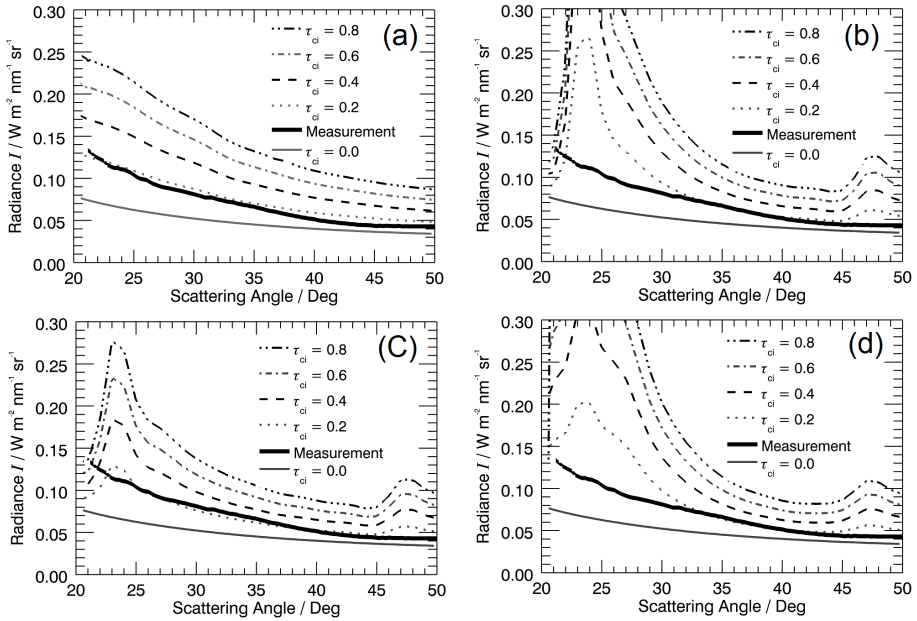

Fig. 10. Measured and simulated $I_{\downarrow}$ as a function of scattering angles. Measurement from 18 April 2011. The simulations were performed for different τ_{ci} and an assumed ice crystal shape of **(a)** rough aggregates, **(b)** solid columns, **(c)** plates, and **(d)** mixture.

AMTD
6, 1201–1238, 2013

Ground-based hyperspectral imaging of cirrus

M. Schäfer et al.

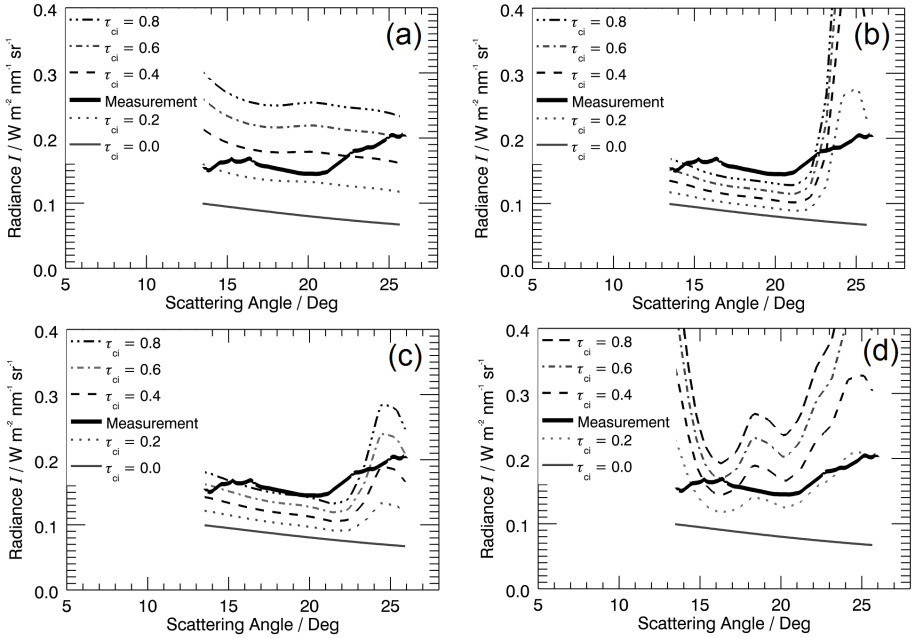

Fig. 11. Measured and simulated $I_{\downarrow}$ as a function of scattering angles. Measurement from 23 April 2011. The simulations were performed for different τ_{ci} and an assumed ice crystal shape of **(a)** rough aggregates, **(b)** solid columns, **(c)** plates, and **(d)** mixture.

AMTD
6, 1201–1238, 2013

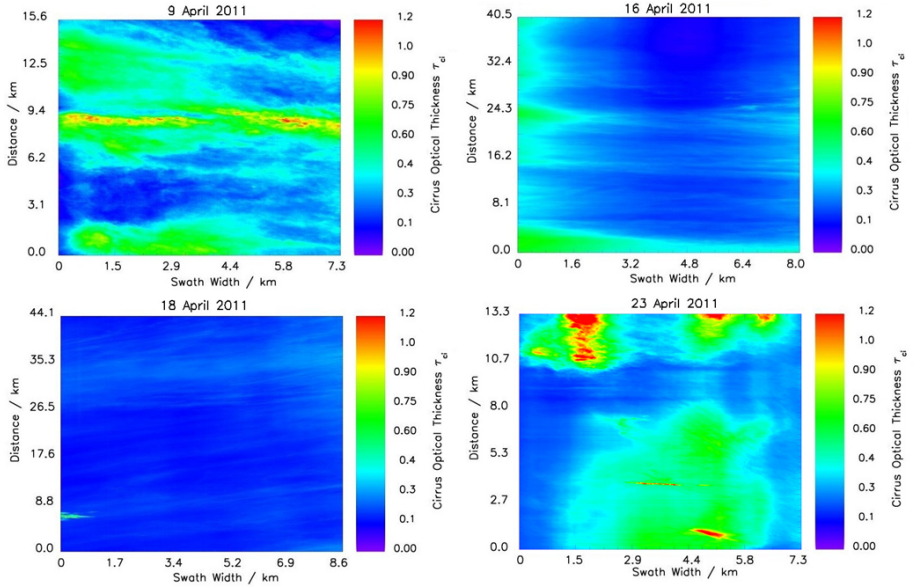

Fig. 12. Time series of the retrieved τ_{ci} during the four measurement cases for each spatial pixel. Abscissa and ordinate values are different due to different measurement conditions.

AMTD
6, 1201–1238, 2013

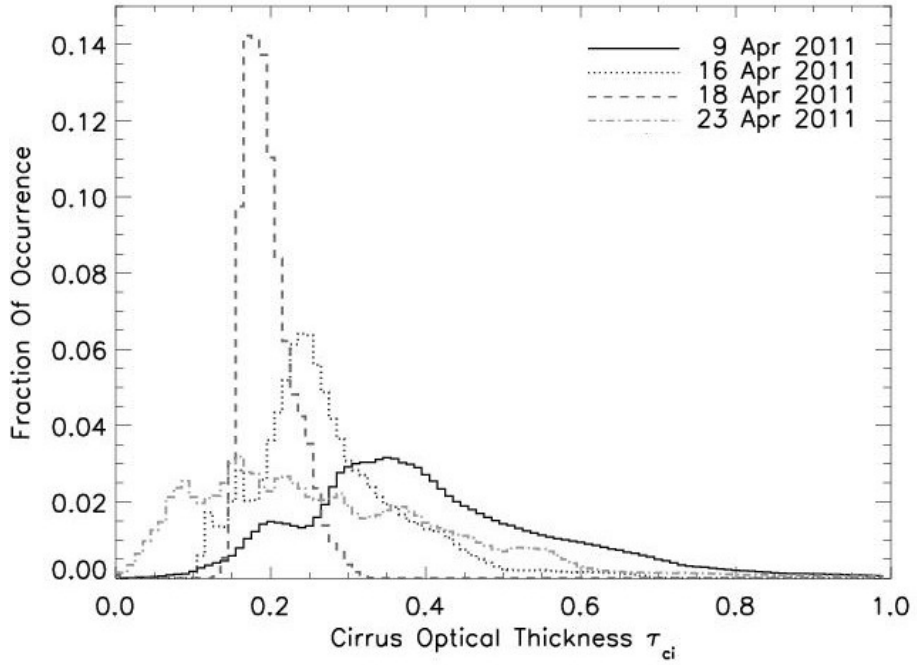

Fig. 13. Normalized histograms of τ_{ci} for each of the four considered measurement days. Bin size is 0.05 in cirrus optical thickness τ_{ci}.

AMTD
6, 1201–1238, 2013

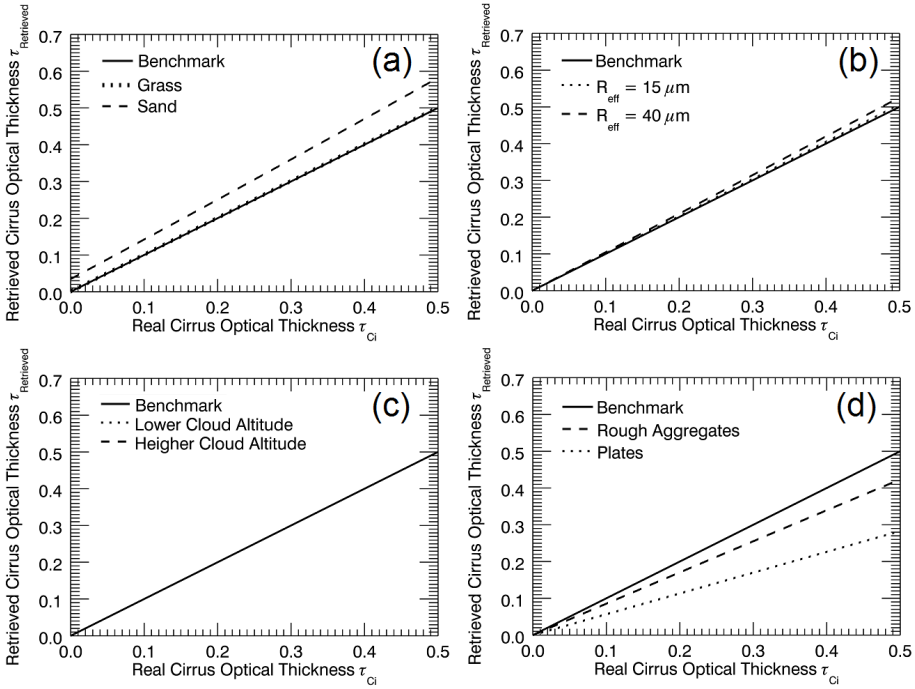

Fig. 14. Retrieval curves for the explanation of the sensitivity results concerning the **(a)** surface albedo, **(b)** effective radius, **(c)** cloud height, and **(d)** ice crystal shape. Calculated for 30° solar zenith angle, 90° solar azimuth angle, solid columns, 11–13 km cloud height, surface albedo for water and 20 µm effective radius. The benchmark case represents the one to one line.

AMTD
6, 1201–1238, 2013